



Identification of Inertial Modes in the Solar Convection Zone

Santiago A. Triana¹ , Gustavo Guerrero^{2,3} , Ankit Barik⁴ , and Jérémy Requier^{1,5} ¹Royal Observatory of Belgium, Ringlaan 3, B-1180 Brussels, Belgium²Federal University of Minas Gerais, Av. Pres. Antônio Carlos, 6627, Belo Horizonte, MG, 31270-901, Brazil³New Jersey Institute of Technology, Newark, NJ 07102 USA⁴Johns Hopkins University, 3400 N. Charles Street, Baltimore, MD 21210, USA⁵Department of Earth and Planetary Science, University of California, Berkeley, CA 94720, USA

Received 2022 April 25; revised 2022 June 13; accepted 2022 June 27; published 2022 July 20

Abstract

The observation of global acoustic waves (p modes) in the Sun has been key to unveiling its internal structure and dynamics. A different kind of wave, known as sectoral Rossby modes, has been observed and identified, which potentially opens the door to probing internal processes that are inaccessible through p -mode helioseismology. Yet another set of waves, appearing as retrograde-propagating, equatorially antisymmetric vorticity waves, has also been observed but their identification remained elusive. Here, through a numerical model implemented as an eigenvalue problem, we provide evidence supporting the identification of those waves as a class of inertial eigenmodes, distinct from the Rossby-mode class, with radial velocities comparable to the horizontal ones deep in the convective zone but still small compared to the horizontal velocities toward the surface. We also suggest that the signature of tesseral-like Rossby modes might be present in recent observational data.

Unified Astronomy Thesaurus concepts: [Astrophysical fluid dynamics \(101\)](#); [Solar oscillations \(1515\)](#); [Solar rotation \(1524\)](#)

1. Introduction

The Coriolis force in any rotating fluid body, from planetary cores and atmospheres to stars, supports the presence of inertial waves. Rossby waves, common in Earth's atmosphere, are a particular subset of inertial waves. In the astrophysical literature, Rossby waves are referred to as r -modes, while the more general class of inertial waves are known, a bit confusingly, as generalized r -modes (Lockitch & Friedman 1999). Rossby waves play a fundamental role in the emission of gravitational waves in neutron stars (Andersson 1998), they have a major influence on Earth's weather (Michel 2011), and may be even present in the fluid cores of terrestrial planets, affecting their global rotation (Triana et al. 2021).

Retrograde-propagating vorticity waves, symmetric with respect to the equator, have been observed and identified a few years ago as Rossby waves in the Sun by Löptien et al. (2018) and further confirmed by Hathaway & Upton (2021) and Gizon et al. (2021). This discovery is highly relevant because the damping rate of Rossby waves is sensitive to turbulent flows, as opposed to the acoustic (p) modes also present in the solar convective zone. Thus, the observation and careful characterization of solar Rossby waves might be instrumental for the understanding of the internal solar dynamics so far elusive for traditional p -mode helioseismology.

More recently, Hanson et al. (2022) provided observational evidence of a distinct set of high-frequency, retrograde-propagating (HFR) vorticity waves, penetrating at least to 3% of the solar radius, but this time with an antisymmetric vorticity with respect to the equator. However, the identification of these waves was left as an open question. They do not seem to fit the

classical Rossby wave dispersion relation that, contrastingly, worked so well for the symmetric-vorticity waves described by Löptien et al. (2018).

In this work, we provide numerical evidence supporting the identification of the HFR waves as a class of inertial waves, different from the Rossby-mode class, that span the whole convective zone depth but with dominant horizontal flows near the outer regions. Our numerical model is based on a simplified physical description of the convection zone, providing the eigenvalues and eigenvectors associated with the inertial modes that it may support.

Nonaxisymmetric (i.e., with azimuthal wavenumber $m \neq 0$) inertial eigenmodes drift in longitude according to their phase speed, so in this work we refer to them as waves or modes interchangeably.

2. A Model For Inertial Eigenmodes

2.1. Main Description

A starting model for solar inertial oscillations can be built by representing the solar convection zone as a spherical shell filled with a homogeneous, incompressible, and viscous fluid. The inner radius r_c of the shell corresponds to the outer radius of the radiative core, with a value $r_c \sim 0.71 R_\odot$ (Christensen-Dalsgaard et al. 1991), R_\odot being the solar radius. The flow velocity associated with the vorticity waves in the convection zone is much smaller than $\Omega_\odot r_c$, where Ω_\odot is a representative value of the Sun's angular speed, thus the flow velocity \mathbf{u} can be described to a good approximation as a small perturbation to the uniformly rotating background flow by the linear Navier–Stokes equation:

$$\partial_t \mathbf{u} + 2\hat{\mathbf{z}} \times \mathbf{u} = -\nabla p + E \nabla^2 \mathbf{u}. \quad (1)$$

The variables in the preceding equation are rendered dimensionless by taking R_\odot and $1/\Omega_\odot$ as the units for length and time, respectively. We use $\hat{\mathbf{z}}$ as the unit vector along the

solar spin axis, and p is the reduced pressure. We introduce also the Ekman number E , defined as

$$E = \frac{\nu_{\text{eff}}}{\Omega_{\odot} r_c^2}, \quad (2)$$

where ν_{eff} is an effective or turbulent eddy viscosity. The flow velocity \mathbf{u} follows a time dependence described by

$$\mathbf{u}(\mathbf{r}, t) = \mathbf{u}_0(\mathbf{r})e^{\lambda t} + \text{cc}, \quad (3)$$

where $\lambda = (\sigma/\Omega_{\odot}) - i(\omega/\Omega_{\odot})$ is a complex number whose real part σ/Ω_{\odot} corresponds to the dimensionless decay rate (or ‘‘damping’’ for short) and the imaginary part ω/Ω_{\odot} to the dimensionless eigenfrequency. We add the complex conjugate (cc) to keep \mathbf{u} real. Then, we write the velocity amplitude \mathbf{u}_0 in the poloidal–toroidal decomposition:

$$\mathbf{u}_0 = \nabla \times \nabla \times [\mathcal{P}(\mathbf{r})\mathbf{r}] + \nabla \times [\mathcal{T}(\mathbf{r})\mathbf{r}], \quad (4)$$

which automatically satisfies the incompressible continuity equation $\nabla \cdot \mathbf{u} = 0$. We use spherical harmonic expansions for the angular dependence of the scalar functions \mathcal{P} , \mathcal{T} . For instance, we write the toroidal scalar function $\mathcal{T}(\mathbf{r})$ as

$$\mathcal{T}(r, \theta, \phi) = \sum_{l=1}^{l_{\text{max}}} \sum_{m=-l}^l T_{lm}(r) Y_l^m(\theta, \phi), \quad (5)$$

where Y_l^m are the spherical harmonics, $T_{lm}(r)$ is a radial function, and l_{max} determines the angular truncation level. A completely analogous expression goes for $\mathcal{P}(\mathbf{r})$. It is sometimes useful to further subdivide the poloidal component into a radial part \mathcal{Q} and a consoidal part \mathcal{S} (known also as ‘‘spheroidal’’). Their spherical harmonic components are written, respectively,

$$Q_{lm} = \frac{l(l+1)}{r} P_{lm}, \quad S_{lm} = \frac{1}{r} \partial_r (r P_{lm}). \quad (6)$$

Note that the horizontal components of the flow velocity are related to both \mathcal{S} and \mathcal{T} , while the radial vorticity is related only to \mathcal{T} .

The spherical harmonic expansion leads to a fully decoupled problem in the azimuthal wavenumber m , allowing us to consider a single m at a time. If $m \neq 0$, inertial eigenmodes are either retrograde or prograde, which is determined by the sign of their phase speed ω/m . Note that the retrograde inertial eigenmode spectrum does not coincide in general with the prograde one. We specify stress-free boundary conditions at both boundaries by requiring

$$\begin{aligned} P_{lm}(r)|_{r=r_b} = P_{lm}''(r)|_{r=r_b} = 0, \\ T_{lm}'(r)|_{r=r_b} - T_{lm}(r)/r|_{r=r_b} = 0, \end{aligned} \quad (7)$$

where r_b denotes the inner or the outer radius of the convective zone and the prime (\prime) symbol denotes the radial derivative.

Our numerical scheme involves expansions of the radial functions $P_{lm}(r)$ and $T_{lm}(r)$ in terms of Chebyshev polynomials. This allows us to write the problem represented by Equation (1) as a generalized eigenvalue problem. For more details, see Appendix A. Solutions can be classified according to their equatorial symmetry, see Appendix B for a brief discussion on the nomenclature.

The use of an incompressible and uniform density fluid in our model might seem too drastic a simplification. However, if the large background density gradient across the convection zone is addressed with the anelastic approximation approach,

Equation (1) would remain almost the same except with \mathbf{u} replaced by $\rho\mathbf{u}$ (thus satisfying $\nabla \cdot \rho\mathbf{u} = 0$, ρ being the fluid density). If the radial displacements are small compared to the horizontal ones, then the difference would be mainly in the viscous term, which has in general only a weak impact on the modes’ frequencies. In fact, even when compared with a fully compressible model that considers a realistic solar density profile (such as Bekki et al. 2022, see their Figure 14), the results of our model differ at most by 15% for $m = 2$, and less than 2% for $m = 16$ Rossby-mode frequencies.

2.2. Choosing a Rotating Frame

In some works, wave frequencies are reported with respect to a reference frame rotating at $\Omega_{\odot}/2\pi = 456$ nHz, known as the Carrington frame (e.g., Gizon et al. 2021; Hathaway & Upton 2021), or using a frame rotating at $\Omega_{\odot}/2\pi = 453.1$ nHz (e.g., Löptien et al. 2018; Hanson et al. 2022). Both rotation rates are close to the mean rotation rate of the solar equator (Larson & Schou 2018). A wave with azimuthal wavenumber m and frequency ω_0 observed in a frame rotating at Ω_0 has a frequency $\omega_1 = \omega_0 + m(\Omega_0 - \Omega_1)$ when observed from a frame rotating at Ω_1 . Throughout the present work, we use the Carrington frame, except where indicated otherwise.

3. Results

The line width Γ of the modes corresponds roughly to two times their decay rate constant σ , in analogy with a lightly damped harmonic oscillator. We have tuned the Ekman number so that the mean $[\sigma]$ of numerically computed modes (the HFR candidates), from $m = 8$ to $m = 14$, matches one-half the mean $[\Gamma]$ of the observed line widths that were computed via ring-diagram analysis of Helioseismic and Magnetic Imager (HMI) measurements, as reported by Hanson et al. (2022; see their Table 1, column 5). Thus, $[\sigma] \approx [\Gamma]/2 = 19.5$ nHz is obtained when $E = 2.1 \times 10^{-4}$. The inertial-mode frequency spectrum is countably dense, so there is always an inertial mode arbitrarily close to any frequency we might choose as a target for the eigensolver. We look for lightly damped modes with a simple spatial structure as they are easier to excite than modes with a more complex structure. The least-damped modes in a broad interval around the observed frequencies are plotted in Figure 1 (blue-violet stars labeled ‘‘HFR, numerical’’). These modes are retrograde-propagating ($\omega < 0$), have equatorially antisymmetric radial vorticity (i.e., equatorially symmetric flow velocity), and their dominant spherical harmonic component, T_{lm} , near the outer boundary is such that $l = m + 1$, matching the corresponding characteristics of the observed HFR vorticity waves. We have extracted the observed HFR frequencies in Figure 1 (orange and deep-pink error bars) from Table 1 and Table S1 of Hanson et al. (2022), transforming them to the Carrington reference frame. For comparison, Figure 1 also presents the sectoral Rossby-mode frequencies obtained with our model, which we used for validation, and the sectoral Rossby modes observed by Löptien et al. (2018). The shaded areas in Figure 1 represent a crude estimate of the effect of the solar differential rotation background on the eigenfrequencies, which we assume is comparable to the variation $\Delta\Omega = \Omega_{\text{max}} - \Omega_{\text{min}}$ of the background rotation rate $\Omega(r, \theta)$ but restricted to the (r, θ) region where a given mode has substantial amplitude. See Appendix C.

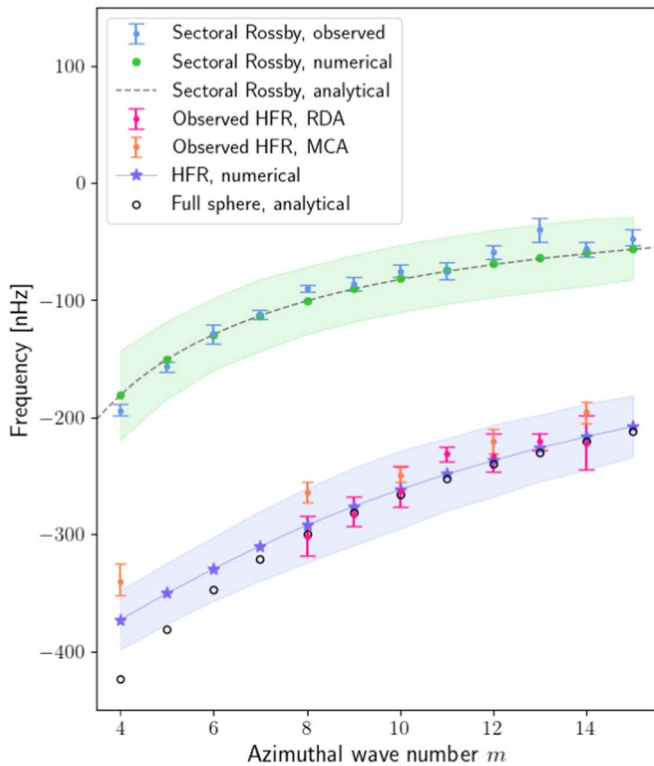


Figure 1. Observed HFR vorticity wave frequencies (relative to the Carrington frame) from mode-coupling analysis (MCA, orange error bars) and from ring-diagram analysis (RDA, deep-pink error bars) compared to numerical inertial-mode frequencies for $E = 2.1 \times 10^{-4}$ and $\delta = 0.29 R_{\odot}$ (blue-violet line with stars). We include observed, numerical, and analytical sectoral Rossby-mode frequencies (as observed in a frame rotating at $\Omega_{\odot}/2\pi = 453.1$ nHz) for reference. Shaded areas represent the possible effect on the eigenfrequencies induced by the solar differential rotation. See main text for further details.

With the exception of the purely toroidal inertial eigenmodes, the eigenfrequencies are sensitive to the radial width of the shell cavity. In Figure 2 we show the eigenfrequencies obtained with our numerical model by considering different convective zone widths δ , and different azimuthal wavenumbers m . Symbol color and size indicates $\log_{10}|\sigma/\Omega_{\odot}|$, with larger, deep-red symbols indicating modes with little damping, which are easier to excite, and smaller, green-turquoise symbols indicating heavily damped modes. We see in the figure eigenmodes with small magnitude frequencies, typically with $|\omega/\Omega_{\odot}| < 0.3$, particularly at low m , with very little damping. For instance, when $m = 4$, the least-damped mode has a frequency of about $\omega/\Omega_{\odot} \sim -0.2$ at $\delta = 0.29 R_{\odot}$ which increases in magnitude for smaller δ . This class of modes has frequencies that generally decrease in magnitude and become more damped as m increases. These are tesseral-like Rossby modes whose frequencies are given to a very good approximation by the dispersion relation (B3) but only when the shell cavity is thin, i.e., when $\delta \lesssim 0.06 R_{\odot}$. The top-left panel in Figure 2 shows the theoretical frequencies of the ($l = 5, m = 4$) and the ($l = 7, m = 4$) Rossby modes from Equation (B3) as horizontal orange dashed lines.

We want to draw attention now to the modes with frequencies near $\omega/\Omega_{\odot} \sim -0.8$ for $m = 4$, $\delta = 0.29 R_{\odot}$, progressively decreasing in magnitude as m increases until reaching $\omega/\Omega_{\odot} \sim -0.45$ at $m = 15$, $\delta = 0.29 R_{\odot}$. With the exception of tesseral-like Rossby modes mentioned earlier, these modes are the least damped in a wide frequency range as

evidenced by their color and symbol size in Figure 2. In the following, we refer to these modes as the main branch. Modes on this branch, and with $\delta = 0.29 R_{\odot}$, are marked with black circles. They appear also in Figure 1 labeled as “HFR, numerical”. A secondary branch, with higher damping and lower frequencies in magnitude, can also be identified. It corresponds to the branch with a mode at $\omega/\Omega_{\odot} \sim -0.55$ (for $m = 4$, $\delta = 0.29 R_{\odot}$). Again, as m increases, their frequency progressively decreases in magnitude until reaching $\omega/\Omega_{\odot} \sim -0.35$ at $m = 15$. Modes on the main branch have the particular property that their toroidal ($l = m + 1, m$) and their consoidal ($l = m, m$) components near the solar surface are dominant, matching the observed waves, while the modes on the secondary branch have a dominant toroidal ($l = m + 3, m$) component near the surface. In Figure 3 we present a side-by-side comparison of the spectral amplitudes near the solar surface ($r = 0.99 R_{\odot}$) between two $m = 8$ modes, one on the main branch (left column panels) and one on the secondary branch (right column panels), for $\delta = 0.29 R_{\odot}$.

Modes in the main branch appear mainly toroidal from the surface, but they harbor a nonnegligible poloidal component deep in the convective zone. The meridional cross sections in Figure 4 (top row) illustrate this point. The color indicates the dimensionless velocity amplitude for each spherical coordinate direction and the amplitude of \mathcal{P} and \mathcal{T} (note that, as a result of an eigenvalue calculation, the overall amplitude of the eigensolution is arbitrary). Modes in the main branch appear to have no radial nodes in the equatorial plane while the modes in the secondary branch (not shown) appear to have one radial node. This suggests that the other weaker branches visible in Figure 2 represent branches with an increasing number of radial nodes.

Lastly, there is a correspondence between the modes in the main branch and a particular class of inertial modes of a full sphere. The inertial modes in a full sphere can be computed analytically (Greenspan 1968; Zhang et al. 2004) and can be specified by three indices (ν, μ, κ), following the notation used by Greenspan (1968). The modes on the main branch reduce (when $\delta = R_{\odot}$) to the only retrograde eigenmodes of the full sphere with $\nu = m + 2$ and $\kappa = m$. These analytical frequencies are plotted in Figure 1 as hollow black circles.

4. Discussion

The inclusion of turbulent viscous diffusion in our model gives us the ability to discern which eigenmodes are more likely to be excited, although it does not tell us anything about the excitation mechanism itself. As explained earlier, we have tuned the Ekman number E in order to match the mean damping rate of the $m = 8, \dots, 14$ eigenmodes in the main branch with one-half of the mean line width of the observed HFR waves. This amounts to an effective viscosity $\nu_{\text{eff}} \simeq 146 \text{ km}^2 \text{ s}^{-1}$. Such relatively large viscosity prevents the appearance of thin internal shear layers that would otherwise appear at low viscosity, ultimately rendering the modes singular in the limit of vanishing viscosity (Rieutord et al. 2001). There is no direct way of measuring the value of the effective viscosity in the solar interior. However, observational and theoretical estimates of the turbulent magnetic diffusivity at the solar surface find values of the order of $100 \text{ km}^2 \text{ s}^{-1}$ (e.g., Baumann et al. 2004; Abramenko et al. 2011; Skokić et al. 2019). Thus, by assuming that the turbulent magnetic Prandtl number is about unity (Käpylä et al. 2020),

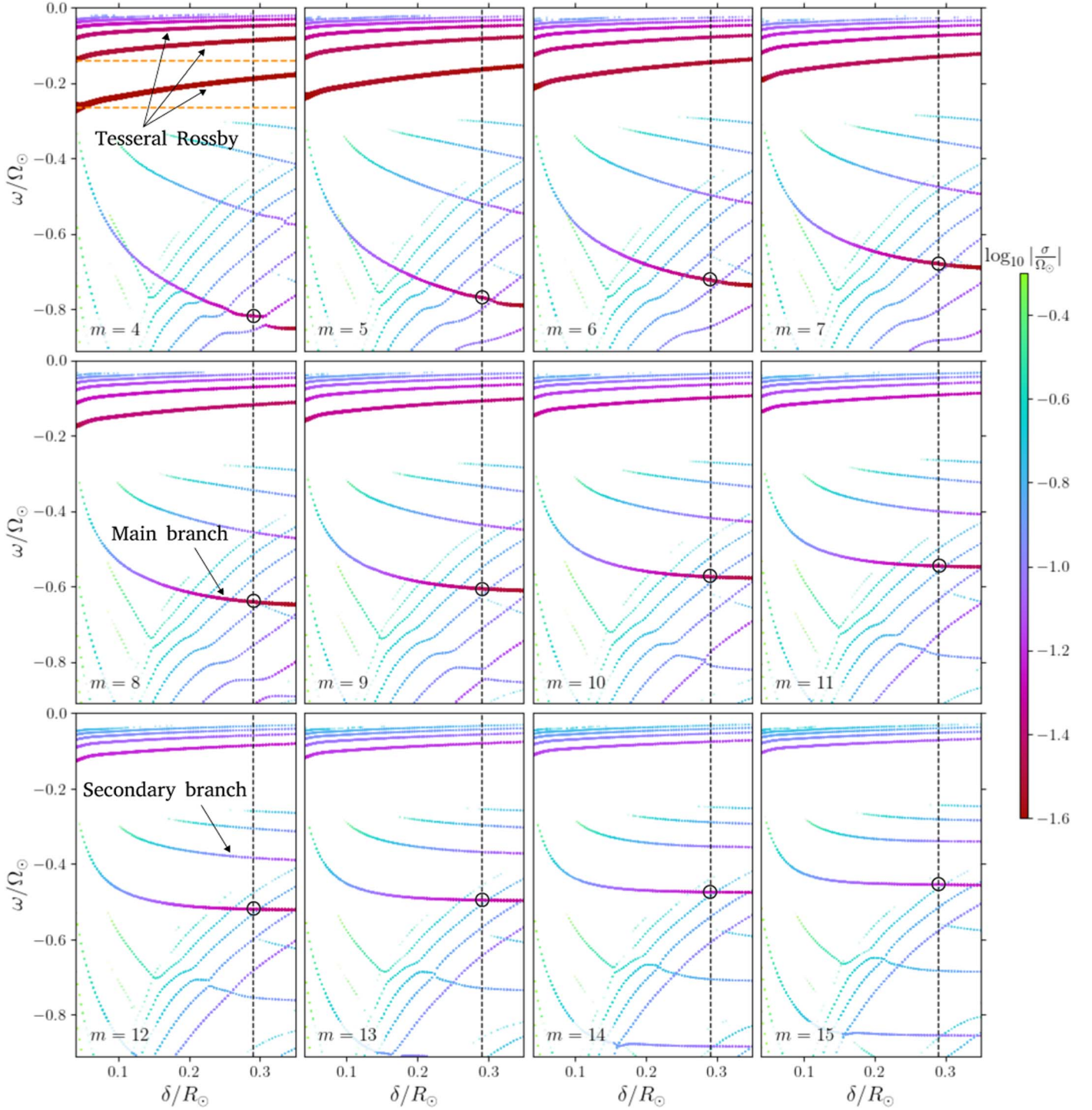


Figure 2. Eigenfrequencies of equatorially antisymmetric vorticity modes as a function of the radial width δ of the convective zone for different azimuthal wavenumbers m . Color and symbol size indicates the eigenmodes' damping decay factor σ with larger deep-red points representing lightly damped modes (more likely to be excited), and smaller green-turquoise points representing heavily damped modes (less likely to be excited). The vertical black dashed line marks the Sun's actual convective zone width at $\delta = 0.29 R_{\odot}$. Black circles mark the modes we identify as the observed HFR waves. The horizontal orange dashed lines in the $m = 4$ panel are the frequencies of the $(l = 5, m = 4)$ and the $(l = 7, m = 4)$ tesseral Rossby modes according to Equation (B3).

our choice is entirely consistent. Furthermore, we can combine the 30 Mm length scale for the large-scale convective flows as proposed by Vasil et al. (2021), with the lower bound of about 10 m/s for the vertical convective velocity as estimated from observations by Greer et al. (2016), resulting in $\nu_{\text{eff}} \simeq 300 \text{ km}^2 \text{ s}^{-1}$. Although within an order of magnitude of our original estimate, the foregoing calculation is admittedly

oversimplified, especially considering that the effective viscosity may be anisotropic and scale dependent (Rincon et al. 2017).

For low- m values ($4 \leq m \leq 8$), the modes we find in the main branch are the second least damped after the tesseral-like Rossby-mode family, while at higher m the main branch becomes the least damped. As shown in Figure 1, the observed

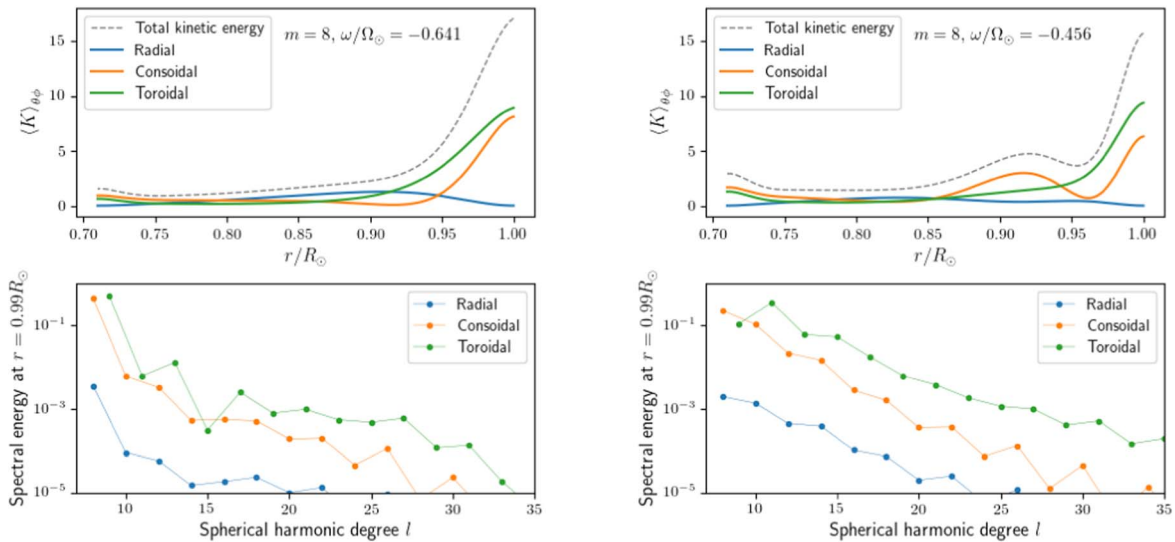


Figure 3. Comparison of two $m = 8$ modes, one on the main branch with $\omega/\Omega_{\odot} = -0.641$ (left column) and one on the secondary branch with $\omega/\Omega_{\odot} = -0.456$ (right column). The top panels show the radial profile of the kinetic energy associated with the radial, consoidal, and toroidal components of the velocity (averaged over θ and ϕ , modes are normalized to have unit kinetic energy). The bottom panels show the fractional energy content of each spherical harmonic component at $r = 0.99 R_{\odot}$ (fractions of the total kinetic energy at that radius). The convective zone width is $\delta = 0.29 R_{\odot}$ and the Ekman number is $E = 2.1 \times 10^{-4}$. Note that the (l, m) spherical harmonic component of the radial vorticity is proportional to $l(l+1)T_{lm}(r)/r$.

HFR wave frequencies as measured in the Carrington frame (rotating at 456 nHz) are a close match to the eigenfrequencies of the inertial modes in the main branch. Note that the sectoral Rossby-mode frequencies shown in Figure 1 are relative to a frame rotating slightly slower at 453.1 nHz. If transformed to the Carrington frame, the sectoral Rossby modes computed from the dispersion relation Equation (B3) would have frequencies systematically smaller than the observations (relative to that frame). The fact that theoretical HFR waves and sectoral Rossby waves both match well the observed frequencies but only when measured in two slightly different rotating frames is most likely a consequence of the different solar rotation rates as “sensed” by the two kinds of waves (see also Appendix C).

Another important piece of evidence is provided by the spherical harmonic components. The eigenmodes in the main branch are characterized by their large ($l = m + 1$, m) spherical harmonic component of radial vorticity near the solar surface (see Figure 3, left column panels), precisely like the observed HFR waves. Note that the consoidal component is also large compared to the radial component near the surface, but the radial vorticity observations are only sensitive to the toroidal component (see Appendix B). Although the toroidal and consoidal components are dominant near the surface, the radial component can be dominant in deeper regions, but never with as much amplitude as the other components near the surface.

It is tempting to adjust δ to match the observed frequencies but it cannot be done consistently for all m numbers. A glance at Figure 2 reveals that modes with low- m numbers are much more sensitive to δ than modes with higher m . However, we cannot rule out entirely the possibility that modes with different m numbers “perceive” a differently sized shell cavity, perhaps related in some way to the meridional circulation pattern in the solar convective zone. Nonetheless, we believe that accounting for the latitudinal differential rotation should be among the first refinements to be investigated.

It is interesting to note that the phase speed frequency $(\omega/2\pi)/m$ of the modes, in the range of 13 to 85 nHz in the

retrograde direction, opens the possibility of co-rotation resonances of the modes with the background latitudinal differential rotation (Baruteau & Rieutord 2013; Guenel et al. 2016). In a reference frame corotating with the solar equator, the latitudinal differential rotation appears as a retrograde azimuthal flow with an angular rotation rate decreasing continuously from $\simeq 120$ nHz near the poles until vanishing at the equator. There is therefore a region in the convective zone in which the Doppler-shifted frequency vanishes for each mode. It is then conceivable that the modes draw their energy from the differential rotation. That being said, there is presumably some kind of interaction between the large-scale convective flow and the inertial waves with comparable time and length scales. In fact, at $m > 15$, the waves appear indistinguishable from convection according to Löptien et al. (2018). Thus, an adequate understanding of the interplay among differential rotation, waves, and large-scale convection is desirable.

The retrograde ($l = m + 1$, m) tesseral-like Rossby modes in our model have rather small damping rates, particularly at low m , which makes them candidates as well to be excited and observed. The power spectra presented by Hanson et al. (2022; see their Figure 1) show indeed some power at low frequencies and low- m numbers in the $l = m + 1$ channel, which might contain the signature of the tesseral-like Rossby modes. Although it is not clear if the observed power in that region is not caused by noise or some other artifact (e.g., sunspots; see Appendix C of Gizon et al. 2021). These tesseral-like Rossby modes have a ratio of toroidal to poloidal kinetic energy much larger than one (a distinguishing feature of all Rossby modes), in contrast to the modes in the main branch. They are mostly columnar, with very little amplitude in the equatorial region as Figure 4 (bottom row) shows. According to our calculations, their spherical harmonic spectra at the surface show significant contributions from the toroidal $l = m + 1$, $m + 3$, $m + 5$, and higher components, which match, at least qualitatively, the data shown in Figure S4 of Hanson et al. (2022).

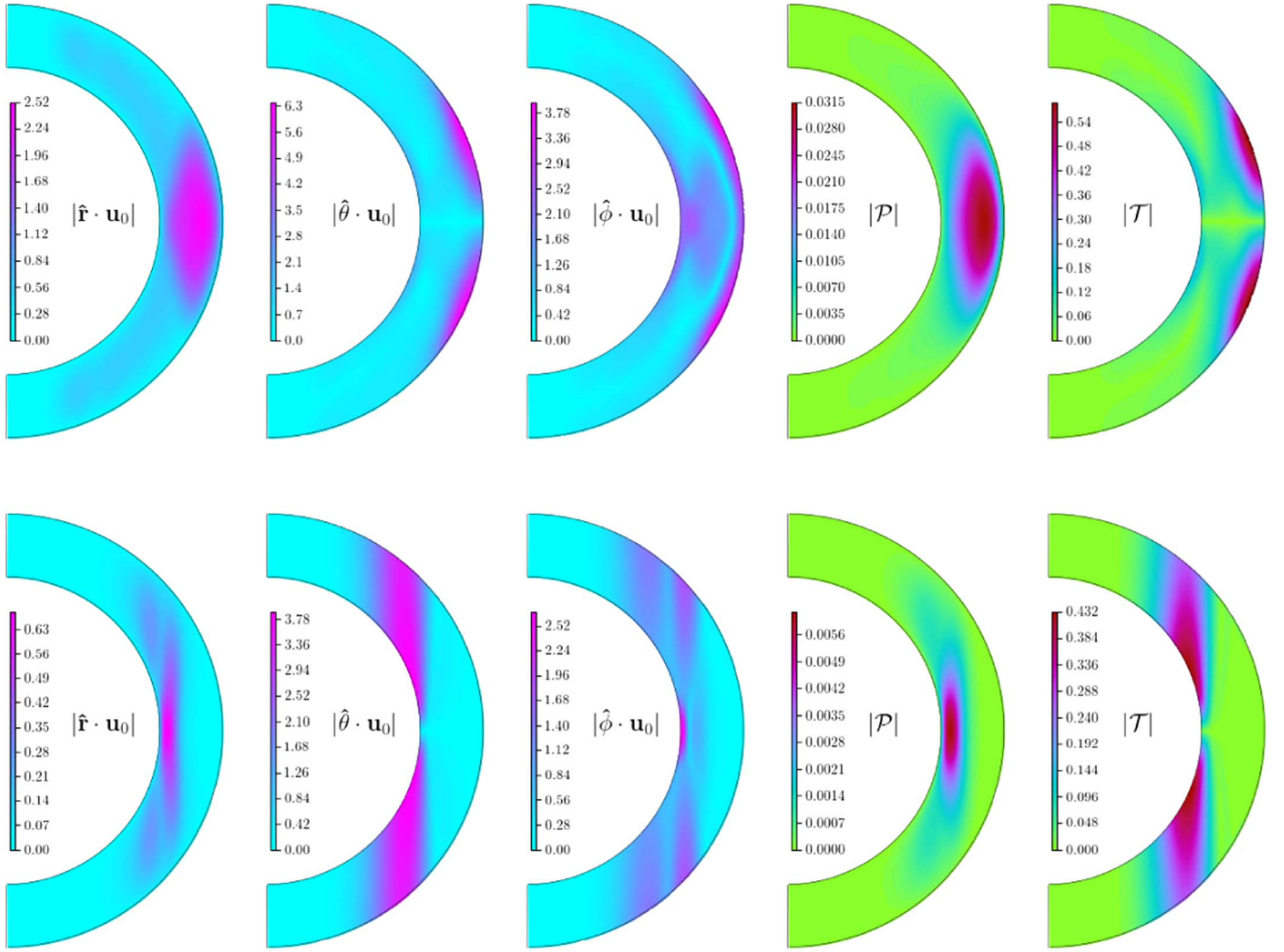


Figure 4. Meridional cross sections of the $m = 8$, $\omega/\Omega_{\odot} = -0.641$ eigenmode on the main branch (top row), and the $m = 8$, $\omega/\Omega_{\odot} = -0.118$ of the tressal-like Rossby-mode family (bottom row). This latter mode is essentially the same as the one reported by Bekki et al. (2022), see their Figure 11(d). Note the absence of radial nodes of \mathcal{P} or $|\hat{\mathbf{f}} \cdot \mathbf{u}_0|$ in the equatorial plane for the main branch mode. The Ekman number here is $E = 2.1 \times 10^{-4}$, and the convective zone width is $\delta = 0.29 R_{\odot}$.

Clearly, the dispersion relation (Equation (B3)) fails to hold for tressal-like Rossby modes in a deep spherical shell, although it still holds for sectoral Rossby modes, regardless of the shell depth. The latter are purely toroidal (i.e., purely horizontal fluid displacements) and their frequency or damping is essentially unaffected by the shell depth. The tressal-like Rossby modes with symmetric vorticity, in addition to the sectoral ones, exhibit similar behavior as the tressal-like Rossby modes with antisymmetric vorticity. As demonstrated by the $m = 4$ panel in Figure 2, their frequency is no longer described by the dispersion relation in Equation (B3), and they become increasingly damped as the shell depth increases. This might explain the apparent lack of symmetric-vorticity modes other than the sectoral Rossby in the analysis by Löptien et al. (2018).

To conclude this section, we note that the Ekman number has a strong influence on the damping rates while only a weak influence on the eigenfrequencies. But even if the Ekman number is reduced by an order of magnitude as shown in Figure 5, the tressal-like Rossby modes and the modes on the main branch persist as the least-damped ones, and the identification of the observed vorticity waves as modes on the main branch remains valid.

5. Summary and Conclusion

We presented evidence supporting the identification of the HFR vorticity waves measured recently by Hanson et al. (2022) as a particular class of inertial modes of a deep spherical shell. Our findings are based on a relatively simple numerical model representing the solar convective zone as a homogeneous, incompressible, and viscous fluid in a rotating spherical shell. The eigenmodes of this system correspond to oscillations where the Coriolis force is the restoring force. We recover the Rossby-mode frequencies described by the well-known dispersion relation (Equation (B3)) but only for sectoral Rossby modes. We find that Rossby modes other than sectoral are also well described by Equation (B3) but only if the depth of the spherical shell is thin compared to its outer radius. Such a thin fluid layer is hardly justifiable for the solar convection zone. Notably, our model also unveils a branch of lightly damped, retrograde-propagating inertial modes with equatorially antisymmetric vorticity, whose dominant spherical harmonic components $T_{lm}(r)Y_l^m$ near the surface are such that $l = m + 1$, and have frequencies close to the wave frequencies observed by Hanson et al. (2022). All of these qualities match

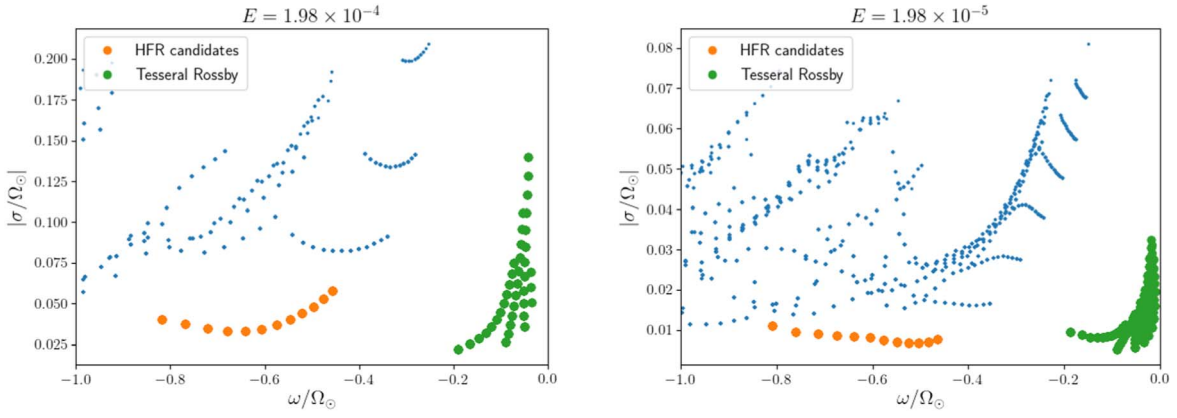


Figure 5. Reducing the Ekman number by an order of magnitude has only a weak influence on the eigenfrequencies ω but a strong one on the damping rates σ . The plot on the left is computed for $E = 1.98 \times 10^{-4}$ and the one on the right for $E = 1.98 \times 10^{-5}$, both for $\delta = 0.29 R_{\odot}$, modes from $m = 4$ to $m = 15$ are included. Even at a reduced Ekman number, the HFR modes (orange dots) remain as the least-damped ones, along with some tesserall-like Rossby modes (green dots). Blue dots represent the remaining inertial modes.

observations, leading us to an unequivocal identification of the HFR waves.

The modes we identify with the HFR waves belong to a class of inertial modes distinct from the Rossby-mode class. Although their toroidal ($l = m + 1$, m) component is much larger than the radial component near the solar surface, their poloidal kinetic energy is still comparable to the toroidal one, as opposed to Rossby modes.

Our numerical calculations also suggest that the signature of low-frequency tesserall-like Rossby modes with antisymmetric vorticity might be present in the observations presented by Hanson et al. (2022). As true Rossby modes, their kinetic energy over the whole convective zone is mostly toroidal, in contrast with the modes in the main branch. Near the solar surface, the tesserall-like Rossby modes have spherical harmonic (l , m) components with contributions from $l = m + 1$, $m + 3$, $m + 5$, and higher orders to a lesser extent, which appears to match the observations as well.

Differential rotation and density stratification are perhaps the most important features missing in our model. However, they are not essential for the identification of the modes. Our aim here is to provide the initial identification of the modes as a starting step toward more refined models, hoping to spark interest from the community in developing inertial-wave models involving differential rotation, magnetic fields, and other effects. Such models, although numerically challenging, are in principle straightforward to develop. More refined inertial-wave models (e.g., Bekki et al. 2022) are potentially very valuable to understand and characterize turbulent processes in the solar convective zone (Gizon et al. 2021), but just as well in the convective zones of other stars where oscillations in the inertial range have been detected (e.g., Ouazzani et al. 2020). Inertial-wave-based helio/asteroseismology has great potential and might give us new insights into the interior dynamics of the Sun and the stars.

S. T. and J.R. express their warm gratitude to Veronique Dehant and Tim Van Hoolst for their encouragement and support. They also acknowledge financial support from the European Research Council (ERC) under the European Union’s Horizon 2020 research and innovation program (Synergy Grant agreement no. 855677 GRACEFUL). A.B. would like to thank Sabine Stanley for her encouragement and

support. J.R. would like to thank Bruce Buffett and UC Berkeley’s Department of Earth and Planetary Science for their hospitality during the writing of this letter. We would like to thank as well Y. Bekki, K. R. Sreenivasan, and two anonymous reviewers for their constructive and insightful comments which helped us immensely to improve this work.

Software: `kore` (Rekier et al. 2019; Triana et al. 2019), SHTns (Schaeffer 2013), PETSc/SLEPc (Balay et al. 1997; Hernandez et al. 2005; Dalcin et al. 2011; Balay et al. 2019; Roman et al. 2022), MUMPS (Amestoy et al. 2001, 2006), Matplotlib (Hunter 2007). We provide `kore` as an open source and freely available code via <https://doi.org/10.5281/zenodo.6783310>. All the data and scripts needed to reproduce all the figures in this work can be found at <https://doi.org/10.5281/zenodo.6787680>.

Appendix A Numerical Method

We expand the poloidal $P_{lm}(r)$ and toroidal $T_{lm}(r)$ functions occurring in Equation (4) using a Chebyshev polynomial basis. We write

$$P_{lm}(r) = \sum_{k=0}^N \alpha_{lm}^k t_k(x), \quad T_{lm}(r) = \sum_{k=0}^N \beta_{lm}^k t_k(x), \quad (\text{A1})$$

where $t_k(x)$ is the Chebyshev polynomial of degree k , N is the radial truncation level, the radial variable is mapped to x via the affine transformation

$$x = 2 \frac{r - r_c}{R_{\odot} - r_c} - 1, \quad (\text{A2})$$

and α_{lm}^k , β_{lm}^k are the unknown coefficients. This is essentially the same technique used by Rieutord & Valdettaro (1997), except that we use a fast spectral method devised by Olver & Townsend (2013). This method uses Gegenbauer polynomial bases to represent the radial derivatives of $t_k(x)$ resulting in sparse matrix operators, as opposed to the spectral collocation method where the operators representing radial derivatives are dense matrices. The resulting matrices representing Equation (1) are banded and sparse. We end up with a generalized eigenvalue problem of the form

$$\mathbf{A}\mathbf{x} = \lambda\mathbf{B}\mathbf{x}, \quad (\text{A3})$$

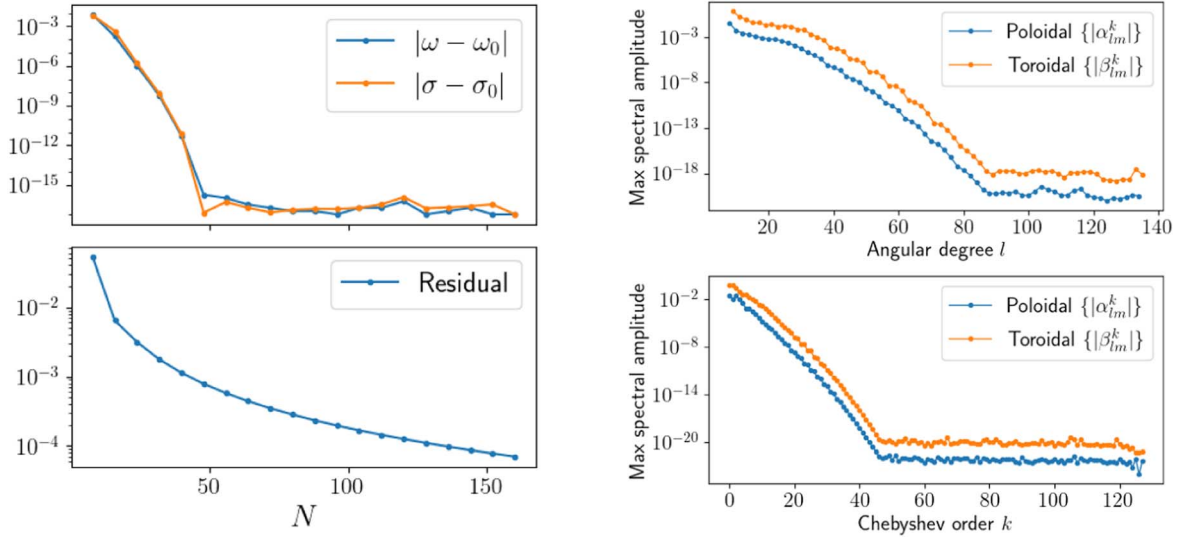


Figure 6. On the top-left panel, we show the effect of changing the truncation level N on the eigenvalue of the $m = 8$, $\omega/\Omega_\odot = -0.641$ eigenmode depicted in Figure 4 as a representative example. The reference eigenvalue $\sigma_0 - i\omega_0$ corresponds to the solution with $N = 160$. The angular truncation l_{\max} is linked to N so that $l_{\max} \sim N$. The bottom-left panel shows the residual (defined in the text). The panels on the right show the maximum magnitude of the Chebyshev coefficients for a given l (top), and for a given k (bottom), associated with a particular solution with $N = 128$, $l_{\max} = 135$.

where \mathbf{A} and \mathbf{B} are sparse matrices, $\lambda = (\sigma - i\omega)/\Omega_\odot$ is the eigenvalue, and \mathbf{x} is the eigenvector comprised by the set of coefficients $\{\alpha_{lm}^k, \beta_{lm}^k\}$. We use a shift-and-invert strategy to obtain solutions with an eigenvalue close to a given target. The truncation levels used in our calculations are typically $N = 156$ and $l_{\max} = 158$ for the radial and angular expansions, respectively.

Figure 6 gives an idea of the accuracy and convergence properties of the method we use. The top-left panel shows the change in the eigenvalue as the truncation level is increased. Machine-precision level on the variation is achieved around $N \sim 50$. A measure of how well Equation (1) is fulfilled is given by the residual plotted on the bottom-left panel. We define the residual as

$$\text{Residual} = \frac{|2\sigma K - \mathcal{D}|}{\max\{|2\sigma K|, |\mathcal{D}|\}}, \quad (\text{A4})$$

where K is the kinetic energy integrated over the whole fluid volume V :

$$K = \frac{1}{2} \int \mathbf{u}_0^\dagger \cdot \mathbf{u}_0 \, dV, \quad (\text{A5})$$

and \mathcal{D} is the viscous dissipation defined as

$$\mathcal{D} = E \int \mathbf{u}_0^\dagger \cdot \nabla^2 \mathbf{u}_0 \, dV. \quad (\text{A6})$$

Our code was designed originally to study the flow in planetary interiors, which typically have very small Ekman numbers and are thus computationally much more demanding compared to the Ekman number associated with the solar convection zone. Our code (named `core`) is freely available as an open-source project: <https://doi.org/10.5281/zenodo.6783310>.

Appendix B Symmetry Considerations

The waves reported by Hanson et al. (2022) are described in terms of the radial vorticity observed near or at the solar

surface. The spherical harmonic coefficients of the radial vorticity at any radius r are related in a simple way to the toroidal functions $T_{lm}(r)$:

$$[\hat{\mathbf{r}} \cdot (\nabla \times \mathbf{u}_0)]_{l,m} = l(l+1) \frac{T_{lm}(r)}{r}. \quad (\text{B1})$$

The velocity field \mathbf{u} of an inertial mode can be either equatorially symmetric or antisymmetric. The vorticity $\nabla \times \mathbf{u}$ has the opposite equatorial symmetry to \mathbf{u} . Explicitly, if a mode is equatorially antisymmetric in the vorticity, it fulfills

$$\begin{aligned} u_r(r, \pi - \theta, \phi) &= u_r(r, \theta, \phi), \\ u_\theta(r, \pi - \theta, \phi) &= -u_\theta(r, \theta, \phi), \\ u_\phi(r, \pi - \theta, \phi) &= u_\phi(r, \theta, \phi), \end{aligned} \quad (\text{B2})$$

i.e., it is equatorially symmetric in velocity. An inertial-mode equatorially symmetric in velocity, with azimuthal wavenumber m , has poloidal functions P_{lm} with indices such that $l = m, m+2, m+4, \dots$, and the toroidal functions T_{lm} have indices such that $l = m+1, m+3, \dots$ conversely when the mode is antisymmetric.

Inertial modes are a general class of modes that include Rossby modes (also known as planetary waves) as a subset. The analytical dispersion relation for Rossby modes, namely,

$$\frac{\omega}{\Omega_\odot} = -\frac{2m}{l(l+1)}, \quad (\text{B3})$$

is usually derived assuming a thin spherical shell, which ignores motion in the radial direction, leaving only the toroidal part (see, e.g., Rieutord 2014). In the ideal case, a Rossby mode has only one spherical harmonic Y_l^m component. These modes can then be classified as sectoral if $l = m$, or tesseral if $l > m$. A sectoral Rossby mode is by necessity equatorially antisymmetric in the velocity (i.e., symmetric in vorticity). These are the modes that have been observed and identified in the Sun by Löptien et al. (2018). Tesseral Rossby modes can have either symmetry. Similarly, a Rossby mode with an equatorially





symmetric velocity (i.e., antisymmetric in vorticity) is thus a tesseral Rossby mode. When the shell is not thin, poloidal motions can become significant, the dispersion relation (B3) is not generally valid, and the foregoing classification does not follow unmodified. Tesseral modes are the most affected, with other spherical harmonics appearing in the solution besides the main tesseral component, although the tesseral component remains dominant. Thus, we call them tesseral like. Sectoral modes are essentially unaffected.

Appendix C Differential Rotation Background

Our model assumes a uniformly rotating background flow. However, we can obtain a crude estimate of the effect of the solar differential rotation background on the eigenfrequencies by considering the range of solar rotation frequencies corresponding to the spatial location (in the r, θ plane) where the amplitude of a given mode is substantial (averaged over ϕ and over an oscillation period). We define the “domain” of a mode as the region where its power is at least one-half of its maximum power, or equivalently, where its amplitude is at least $\sqrt{2}/2$ times its maximum amplitude. We compute then the difference $\Delta\Omega = \Omega_{\max} - \Omega_{\min}$ between the maximum and minimum solar rotation rate (based on Larson & Schou 2018) within the mode’s domain. The shaded areas in Figure 1 represent $\omega \pm \Delta\Omega$, where ω is the mode’s frequency from the uniformly rotating model.

Note that if a mode has a substantial amplitude only in regions where the solar rotation rate can be considered constant, say Ω_0 , then we expect no effect on the eigenfrequency, i.e., the uniform rotation model would be accurate, provided the frequency is referred to a reference frame rotating at Ω_0 .

ORCID iDs

Santiago A. Triana  <https://orcid.org/0000-0002-7679-3962>
 Gustavo Guerrero  <https://orcid.org/0000-0002-2671-8796>
 Ankit Barik  <https://orcid.org/0000-0001-5747-669X>
 Jérémy Requier  <https://orcid.org/0000-0003-3151-6969>

References

Abramenko, V. I., Carbone, V., Yurchyshyn, V., et al. 2011, *ApJ*, 743, 133

- Amestoy, P. R., Duff, I. S., L’Excellent, J.-Y., & Koster, J. 2001, *SIAM J. Matrix Anal. Appl.*, 23, 15
- Amestoy, P. R., Guermouche, A., L’Excellent, J.-Y., & Pralet, S. 2006, *ParC*, 32, 136
- Andersson, N. 1998, *ApJ*, 502, 708
- Balay, S., Abhyankar, S., Adams, M. F., et al. 2019, *PETSc Users Manual, Tech. Rep. ANL-95/11—Revision 3.11*, Argonne National Laboratory
- Balay, S., Gropp, W. D., McInnes, L. C., & Smith, B. F. 1997, in *Modern Software Tools in Scientific Computing*, ed. E. Arge, A. M. Bruaset, & H. P. Langtangen (Boston, MA: Birkhäuser Press), 163
- Baruteau, C., & Rieutord, M. 2013, *JFM*, 719, 47
- Baumann, I., Schmitt, D., Schüssler, M., & Solanki, S. K. 2004, *A&A*, 426, 1075
- Bekki, Y., Cameron, R. H., & Gizon, L. 2022, *A&A*, 662, A16
- Christensen-Dalsgaard, J., Gough, D., & Thompson, M. 1991, *ApJ*, 378, 413
- Dalcin, L. D., Paz, R. R., Kler, P. A., & Cosimo, A. 2011, *AdWR*, 34, 1124
- Gizon, L., Cameron, R. H., Bekki, Y., et al. 2021, *A&A*, 652, L6
- Greenspan, H. 1968, *The Theory of Rotating Fluids*, Cambridge Monographs on Mechanics (Cambridge: Cambridge Univ. Press)
- Greer, B. J., Hindman, B. W., & Toomre, J. 2016, *ApJ*, 824, 128
- Guenel, M., Baruteau, C., Mathis, S., & Rieutord, M. 2016, *A&A*, 589, A22
- Hanson, C. S., Hanasoge, S., & Sreenivasan, K. R. 2022, *NatAs*, 6, 708
- Hathaway, D. H., & Upton, L. A. 2021, *ApJ*, 908, 160
- Hernandez, V., Roman, J. E., & Vidal, V. 2005, *ACM Trans. Math. Software*, 31, 351
- Hunter, J. D. 2007, *CSE*, 9, 90
- Käpylä, P. J., Rheinhardt, M., Brandenburg, A., & Käpylä, M. J. 2020, *A&A*, 636, A93
- Larson, T. P., & Schou, J. 2018, *SoPh*, 293, 29
- Lockitch, K. H., & Friedman, J. L. 1999, *ApJ*, 521, 764
- Löptien, B., Gizon, L., Birch, A. C., et al. 2018, *NatAs*, 2, 568
- Michel, C., & Rivière, G. 2011, *JATIS*, 68, 1730
- Olver, S., & Townsend, A. 2013, *SIAMR*, 55, 462
- Ouazzani, R.-M., Lignièrès, F., Dupret, M.-A., et al. 2020, *A&A*, 640, A49
- Requier, J., Trinh, A., Triana, S., & Dehant, V. 2019, *GeoJI*, 216, 777
- Rieutord, M. 2014, *Fluid dynamics: an introduction* (Berlin: Springer)
- Rieutord, M., Georgeot, B., & Valdetarro, L. 2001, *JFM*, 435, 103
- Rieutord, M., & Valdetarro, L. 1997, *JFM*, 341, 77
- Rincon, F., Roudier, T., Schekochihin, A., & Rieutord, M. 2017, *A&A*, 599, A69
- Roman, J. E., Campos, C., Dalcin, L., Romero, E., & Tomas, A. 2022, {SLEPC} Users Manual DSIC-II/24/02 - Revision 3.17, Universitat Politècnica de València
- Schaeffer, N. 2013, *GGG*, 14, 751
- Skokić, I., Brajša, R., Sudar, D., Ruždjak, D., & Saar, S. 2019, *ApJ*, 877, 142
- Triana, S. A., Dumberry, M., Cébron, D., et al. 2021, *SGeo*, 43, 107
- Triana, S. A., Requier, J., Trinh, A., & Dehant, V. 2019, *GeoJI*, 218, 1071
- Vasil, G. M., Julien, K., & Featherstone, N. A. 2021, *PNAS*, 118, e2022518118
- Zhang, K., Liao, X., & Earnshaw, P. 2004, *JFM*, 504, 1